4D Printing of NiTi Auxetic Structure with Improved Ballistic Performance

Hassanin, H.

4D Printing of NiTi Auxetic Structure with Improved Ballistic Performance

Hany Hassanin [1], Alessandro Abena[2], Mahmoud Elsayed [3], and Khamis Essa [2]

1 School of Engineering, Canterbury Christ Church University, Canterbury, CT1 1QU, UK

2 University of Birmingham, Birmingham, B15 2TT, UK

3 Department of Industrial and Management Engineering, Arab Academy for Science and Technology and Maritime Transport, P.O box 1029, Abu Qir, Alexandria 21599, Egypt.

The authors declare no conflict of interest

Abstract

Auxetic structures have attracted attention in energy absorption applications owning to their improved shear modulus and enhanced resistance to indentation. On the other hand, Fourdimensional (4D) printing is an emerging technology that is capable to 3D print smart materials with additional functionality. This paper introduces the development of NiTi negative Poisson's ratio structure with superelasticity/shape memory capabilities for improved ballistic applications. An analytical model was initially used to optimise the geometrical parameters of a re-entrant auxetic structure. It was found that re-entrant auxetic structure with a cell angle of -30° produced the highest Poisson's of -2.089. 4D printing process using powder bed fusion system was used to fabricate the optimised NiTi auxetic structure. The measured negative Poisson's ratio of the fabricated auxetic structure was found in agreement with both the analytical model and the finite element simulation. A finite element model was developed to simulate the dynamic response of optimised auxetic NiTi structure subjected to different projectile speeds. Three stages of the impact process describing the penetration of the top plate, auxetic structure, and bottom plate have been identified. The results show that the optimised auxetic structures affect the dynamic response of the projectile by getting denser towards the impact location. This helped to improve the energy absorbed per unit mass of the NiTi auxetic structure to about two times higher than the solid NiTi plate and five times higher than the solid conventional steel plate.

Keywords: *4D printing; NiTi; shape memory alloy; super elasticity; Auxetic*

1. Introduction

Metamaterials have attracted substantial research interest attention during the past few years as an emerging concept to develop materials with novel properties different from

conventional materials, for example, such as negative compressibility, negative Poisson's ratio, manipulating electromagnetic radiation or sound waves and negative elasticity. The macro/micro structure of this type of materials can be tuned to achieve desirable physical or mechanical properties, and therefore, metamaterials are also considered as designed materials. Auxetic materials, one of the metamaterials, possess a negative Poisson's ratio, which is the ratio of longitudinal strain to the transverse strain when the material is stretched longitudinally. The Poisson's ratio value is positive for any conventional materials. This leads to improved shear modulus, stiffness, enhanced resistance to indentation, and improved impact energy absorption. Examples of naturally found auxetic materials include zeolites minerals, cow skin, cancellous bone, and tendons [1-3]. There has been a wide range of applications in using auxetic structures to develop products with desirable functionalities such as bioprostheses shape memory foams, and running shoes. The benefits of using auxetic structures in these applications are not only because of their improved mechanical behaviour but because they also hold properties, for example, enhanced energy absorption, shear resistance, and a higher indentation resistance [46]. This has led to the advancement of auxetic metamaterials especially with the emerging of additive manufacturing (AM) which allowed designers to have the geometrical freedom to fabricate structures with complex and controlled macro/micro-structure.

Auxetic structures can be classified into categories according to their deformation mechanism or geometry. There are three basic structures of auxetic materials: chiral structures, re-entrant structures, and rotating rigid structures. Among them, re-entrant auxetic structures are considered the most important especially when manufactured from high ductility material. Reentrant structures exhibit high stability, high load-carrying capacity, and high ductility under dynamic loading [7-9].

Several research studies explored the design of auxetic materials and their behaviour under high-speed impact projectiles. Schultz et al. [10] studied auxetic structures under blunt impact

projectiles similar to those used in tennis balls launchers. Four structures were produced, two with standard honeycomb hexagonal geometry whereas the other two were with re-entrant geometry. The four structures were subjected to projectile impact with different velocities. The results showed that the auxetic structures with re-entrant unit cells absorbed impact energy higher than honeycomb ones. In addition, the re-entrant structure with greater cell angle showed a high ballistic limit greater than 50 m/s [10]. Qi et al. [11] studied the ballistic limit and the energy absorption capability of auxetic sandwich structures. A finite element modelling was developed, in which a projectile with a set of velocities was used on three different panels configurations: rectangular, hexagonal, and auxetic structures. The authors found that panels with auxetic structures have the highest ballistic limit of 190 m/s followed by hexagonal and rectangular structures, which had ballistic limits of 175 and 161 m/s, respectively. These results suggested that Auxetic structures have great potential in ballistic applications compared to conventional structures [11]. Recently, a similar study was introduced by Imbalzano et al. [12]. They numerically investigated the use of several sandwich panels with cores made of auxetic structure between two metal sheets for high-speed projectile applications. They carried out a parametric study to assess the effect of the panels configuration on the ballistic performance. The energy dissipation and deformations of the panels were assessed against conventional solid panels with the same material and equivalent mass. The study found that the auxetic panels improved the ballistic limit to about 200 m/s with a reduced deformation of 56% [12].

Different materials have been considered in the fabrication of auxetic structures for ballistic applications such as steel, aluminium, and titanium. Titanium alloys were found to have superior ballistic performance when compared to steel. This is because Titanium alloys have low density and high strength-to-weight ratio. Gooch et al. [13] investigated the ballistic capabilities of panels made of different materials. The study found that titanium alloy has impact energy absorption 1.3 times higher than steel [13].

Several manufacturing approaches are available to fabricate auxetic structures depending on the processed material and the intended application. Auxetic polymeric foams are typically produced using compression, heating, cooling and relaxation of conventional foam [14]. A modified method was introduced by Webber et al. which includes a compaction process followed by two steps sintering processes to prepare auxetic polyethylene [15]. Composite auxetic materials such as carbon fibre reinforced polymer (CFRP) were produced using the conventional assembly method [16]. Lithographic processes such as soft lithography are also employed to prepare metal and ceramic auxetic structures [17, 18], though these techniques were originally used for MEMS manufacturing [19-29].

Additive manufacturing or 3D printing is a technology to create objects layer by layer using a 3D printer according to a digital model. The technology enables the processing of metals [3033], ceramics [34], polymers [35], and composites [36] has been widely employed in many industries, such as biomedical [37], defence [17], aerospace [38, 39], energy [40]. The ability of AM to process a wide range of materials into objects with intricate geometries such as auxetic and cellular structures and to obtain desired mechanical properties has led to the many advancements of this technology. Four-dimensional (4D) printing is one form of 3D printing techniques that has been progressed further to process materials that have the ability responds to external stimuli, which offers products with added functionality that can be triggered without human or computer interaction. 4D printing offers several advantages such as the ability to produce smart products that can change their geometries when required [17]. Choong et al. [41] used stereolithography to process photopolymer containing tBA-co-DEGDA network with rapid curing and shape memory effect. The authors extended the study and fabricated silica reinforced shape memory to achieved better mechanical properties and a shape recovery ratio of 87–90% [42].

Powder Bed Fusion (PBF), which is also known as Selective Laser Melting, is a key powder bed AM that can process a wide range of metal alloys with complex structures. Recently PBF

has become widely adopted in many industrial applications offering advantages when compared to traditional manufacturing such as versatility, accuracy as well as the ability to produce functional components. The technology demonstrated a great capability to process NiTi with high repeatability [43, 44]. To improve the functionality of auxetic materials, shape memory alloys (SMA) such as NiTi can be used to combine the properties of the material to the unique behaviour of the structure. NiTi SMAs exhibits motor-functionalities due to a reversible phase transformation from martensite to austenite and vice versa which can be triggered by temperature (shape memory effect) or deformation (superelasticity). This motorfunctionality makes NiTi suitable for energy-absorption, actuating and inflatable devices, as they can be actuated to their initial shape when deformed, with or without the aid of external heat [45].

This study aims to introduce a new metamaterial that combines the properties of NiTi and auxetic materials in one structure which is processed using 4D printing. The main objectives are to design, simulate, and fabricate NiTi re-entrant structures for improved ballistic performance. Analytical and FEA models were constructed and validated against the fabricated structure when subjected to compressive tests. The FEA model was then used to assess the capability of using NiTi and auxetic structure when subject to a high-speed projectile impact.

2. Methodology

2.1.Analytical Calculations

In-plane analytical calculations were carried out on a re-entrant auxetic structure in order to obtain a high negative Poisson's ratio before FEA modelling. Next, FEA and experimental analysis will be conducted to verify the optimisation calculations. A high negative Poisson's ratio is desirable as it enhances the associated ballistic capabilities. The geometry of the reentrant structure is presented in Figure 1. The geometrical parameters of the re-entrant cell are thickness , the internal angle ∅, the length , and height [46].

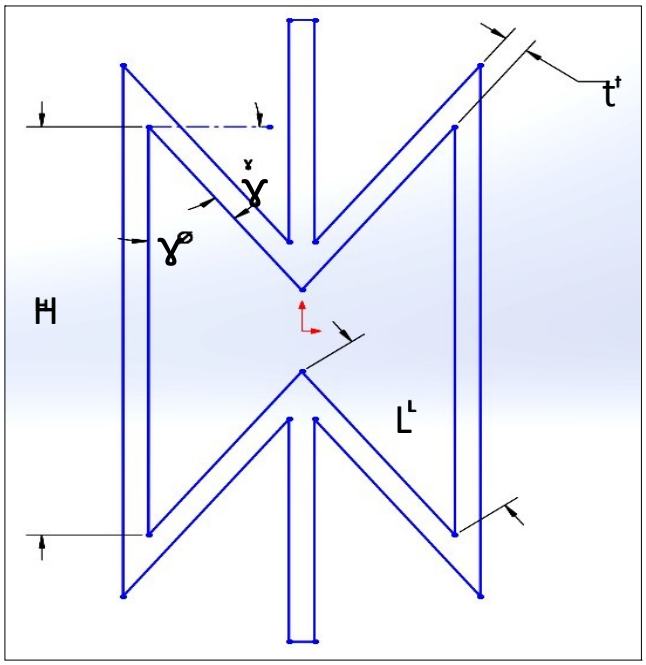

Figure 1: Configuration of the re-entrant unit cell

An analytical equation of the Poisson's ratio of the re-entrant unit cell, introduced by Gibson and Ashby [47], was used in this study. The Poisson's ratio equation is in terms of axial and transverse deformation is given by:

$$\nu = \left(\frac{\cos^2\gamma}{\alpha + \sin\gamma}\right)\left(\frac{1-\beta^2}{\sin\gamma_1 + \beta^2\cot^2\gamma}\right) \quad (1)$$

where is the aspect ratio (/), is the ratio (/), and = 90°−∅. For auxetic structures, a geometric requirement must be added to make sure that the vertices do not overlap during deformation, which is:

$$\gamma_{min} = \sin^{-1}\left(- \alpha_2\right) \quad (2)$$

In this study, the analytical model was employed to study the influence of unit cell geometrical parameters (, , , and γ) on the Poisson's ratio. Table 1 shows the geometrical

parameters and the range of each one of them considering their manufacturability using PBF [10]. For each set of the cell dimensions, and were calculated first along with the value of γ before calculating the corresponding in-plane Poisson's ratio.

Table 1: Re-entrant unit cell geometrical parameters and its corresponding ranges

Parameter	Min. value	Max. value
H (mm)	2	4
L (mm)	2	3
t (mm)	0.2	0.5
γ (deg.)	-70	-30

2.2.Modelling of Compression Testing

The auxetic structure subjected to a compression loading was modelled using FEA and the Poisson's ratio was calculated and validated experimentally. The optimum geometrical parameters of the re-entrant unit cell that generate the highest in-plane negative Poisson's ratio using the analytical model were implemented. The model was first designed using SolidWorks and then the digital model was imported into LS-DYNA for post-processing. The model consists of 5 by 5 unit cells at each face. A schematic diagram of the auxetic structure is shown in Figure 2.

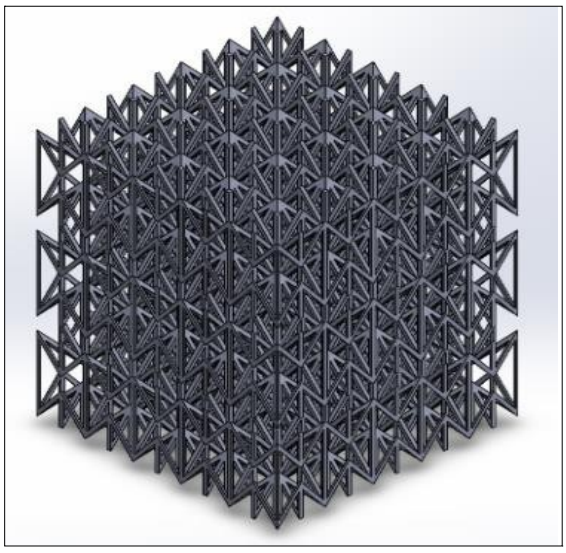

Figure 2: The isometric view of the optimised model

The model was meshed into solid type elements with a dimensional size of 0.52 mm. The properties of the NiTi alloy was employed using shape memory card which provides the material behaviour when undergoes a large deformation [48, 49], see Table 2. A fixed constraint was applied at the bottom of the structure to restrict its movement and a compressive load was employed using a maximum displacement of 1mm at the top surface of the structure.

Table 2: Properties of NiTi shape memory alloy [48, 49]

Melting point (°C)	1300
Young modulus (GPa)	29.3
Density (g/cm^3)	6.45
Poisson's ratio	0.33
$\sigma^{AS}{}_{F}$ (MPa)	896
$\sigma^{AS}{}_{S}$ (MPa)	790
$\sigma^{AS}{}_{S}$ (MPa)	600
$\sigma^{AS}{}_{F}$ (MPa)	450
[a]ε_1	0.078
[b]ε_2	0.08
[c]α	0
[d]ΔE	0
[e]ε_{pmax}	0.175

a. ε_1 is the strain at the end of martensite to austenite transformation

b. ε_2 is the strain at the end of austenite to austenite transformation.

c. α is a parameter measuring the difference between material responses in tension and compression (set α= 0 for no difference).

d. ΔE is Young's modulus for the martensite phase if is different from the modulus for the austenite. Set to zero if equal to the austenite modulus

e. ε_{pmax} is the maximum principal strain at failure.

2.3.4D Printing and Characterization

NiTi ingot was argon atomised into spherical powder with d_{50} of 65 μm by (TLS Technik, Germany), Figure 3a. Concept Laser M2 PBF system with an oxygen-content <0.1% was used in the fabrication process. The auxetic structure was 4D printed using a volumetric

energy density of 300 J/mm^3, power of 70 watts, and a layer thickness of 20 µm. Differential Scanning Calorimetry (DSC) using Mettler DSC 25 was carried out in an Ar atmosphere to study the phase transformation of the fabricated sample for up to a temperature of 120ϑ°C. The fabricated samples were characterised using a Zwick Roell machine to investigate the compressive properties. Lubricated papers were used on the bottom clamping surface to reduce friction. The friction coefficient of the lubricated paper was measured and was found as 0.1. A preload of 50 N and a compression displacement speed of 1 mm/min were set. The axial and transverse displacement of the auxetic structure was recorded during loading. Figure 3b shows the samples under compression testing.

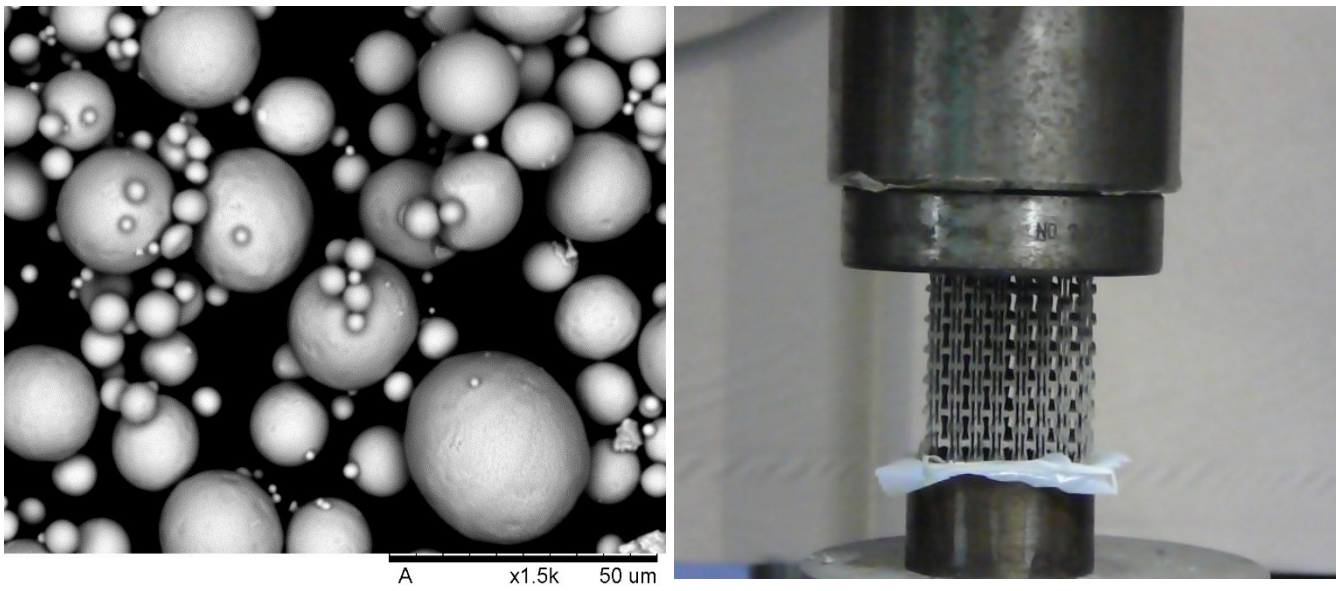

Figure 3: (a) SEM of the NiTi powder, (b) the fabricated auxetic structure under compression testing.

2.4.Modelling of Ballistic Limit

Finite element analysis was performed in order to investigate the performance of the optimised auxetic structures made of NiTi under the high-speed projectile impact. A comparison study with a typical solid steel alloy and NiTi plates was firstly performed to understand the role of the superelasticity of the NiTi on the ballistic properties. The use of

solid mild steel plate has been investigated by several researchers and therefore, the model can be validated against experimental data from the literature. Next, the optimised NiTi auxetic model was carried out to calculate the performance against high-speed projectiles. Ls-Dyna software was used to carry out the numerical simulation. Additionally, MSC Patran, ETA FEMB and LS-PrePost were used in the pre-processing stage.

The projectile considered in the study was the 7.62 mm APM2, which is made of a core of hard steel, a brass jacket, and a lead cap. The projectile was modelled with and without the jacket and cap. It was found that modelling only the core without the other two elements of the projectile, the jacket and the cap did not significantly affect the simulation results. This is in agreement with the literature [50] as the study found that the jacket and cap can only reduce the ballistic velocity by 3-5%. As a result, only the steel core was considered in the following calculations to reduce computational time. The core dimensions are 27.6 mm long, 6.2 mm in diameter, and weighed 5.2 g [51]. The hard steel properties of the core are reported in Table 3. The projectile is considered as rigid similar to reference [52].

The steel plate used in this study has a square geometry with dimensions of 200 mm x 200 mm and a thickness of 4.7 mm [51]. A mesh dependence study [53] was carried out based on published experimental results [51]. It was found that 3D solid elements with $1/6^{th}$ of plate thickness were able to satisfactorily represent the plate behaviour. However, in order to develop a more accurate model able to correctly represent the impact process with a more realistic prediction of the target damage, a finer mesh was used in the impact region. Elements near the impact zone with 0.5x0.5 mm in-plane dimension and 0.52 mm thickness were used. The dimension of these elements was increased with increasing the distance from the impact point.

The plate was eliminated from the calculation when the failure strain value was reached.

Table 3: Properties of the core and the solid plate, [50]

Material	Density [kg/m^3]	Young's Modules [GPa]	Poisson's ratio	Yield stress [MPa]	E_{tan} [GPa]
Hard steel	7850	203.4	0.30		
Mild steel	7810	205.4	0.30	205	80

The contact algorithm has to set correctly in order to represent the real condition during the impact. Contact eroding surface to surface contact algorithm was implemented as suggested in [54]. In addition, friction and heat were not considered in the modelling. Time step is one of the important tools in dynamic impact simulations. Since the velocity value considered in the present analysis is very high, the time step has to be small enough to allow the correct execution of the analysis, for instance, to avoid overlap between the projectile and the plate elements during the contact. The control time step was implemented within Ls-Dyna code similar to the literature [50].

In order to implement an appropriate hourglass control in the model, the data shown in [54] was used. A stiffness hourglass control is suggested for metals setting IHQ=4, and considering an hourglass coefficient QH=0.03. A comparison between the evolved internal and hourglass energy had to be performed in order to check that the model calculations are reliable. It is suggested that the model can be considered consistent if hourglass energy is < 10 % of internal energy peak [10]. The developed model of the projectile and the solid plate is shown in Figure 4.

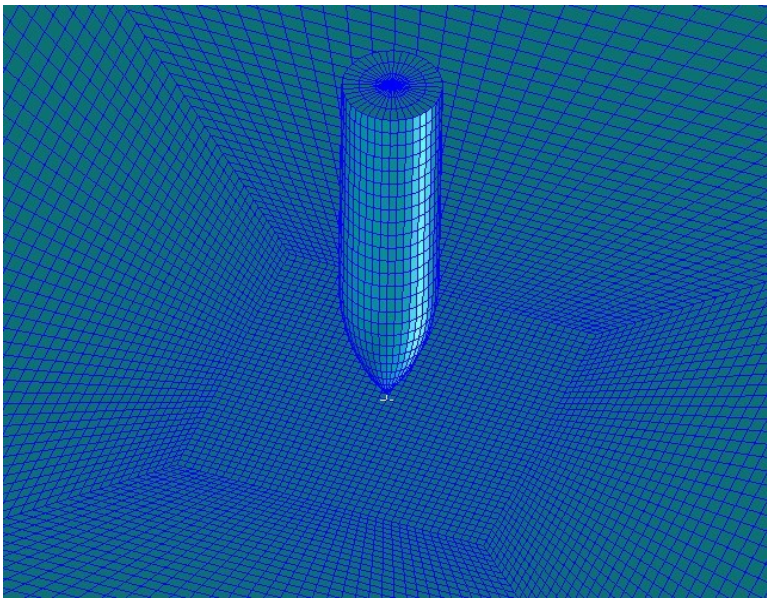

Figure 4: The numerical model of the projectile and solid plate.

The next step is to replace steel with the NiTi alloy. The typical behaviour of shape memory alloy material is presented in Figure 5a. NiTi properties were implemented based on the data published in [55] and as shown in Table 2. The Ls-Dyna material card, which can be used to describe the material behaviour shown in Figure 6a. The condition for element failure and elimination is set (maximum principal strain at failure). Following the simulation of solid NiTi plate subjected to a high-speed projectile, the solid NiTi plate was replaced with a re-entrant Auxetic structure with two facets on the top and bottom, as shown in Figure 5b,c. The auxetic structure was 20 mm high whereas the top and bottom facets have 2 mm thickness.

The Auxetic structure with two facets made of NiTi was manufactured in one step using concept laser M2. A striking face followed by a back face is commonly used in armouring systems. It was aimed to be thin in order to understand the role of the auxetic structure and how it behaves during penetration. Facets thickness of 2mm were found suitable for manufacturability. We avoided using shorter structure to allow the auxetic structure to deform and behave in an auxetic way. In our calculations, we used energy per unit mass to minimise the effect of the size of the structure. The ballistic limit was calculated using an impact speed steps of 5m/s increase until zero residual velocity was achieved. The speed step was refined to

±1m/s to improve accuracy [56].

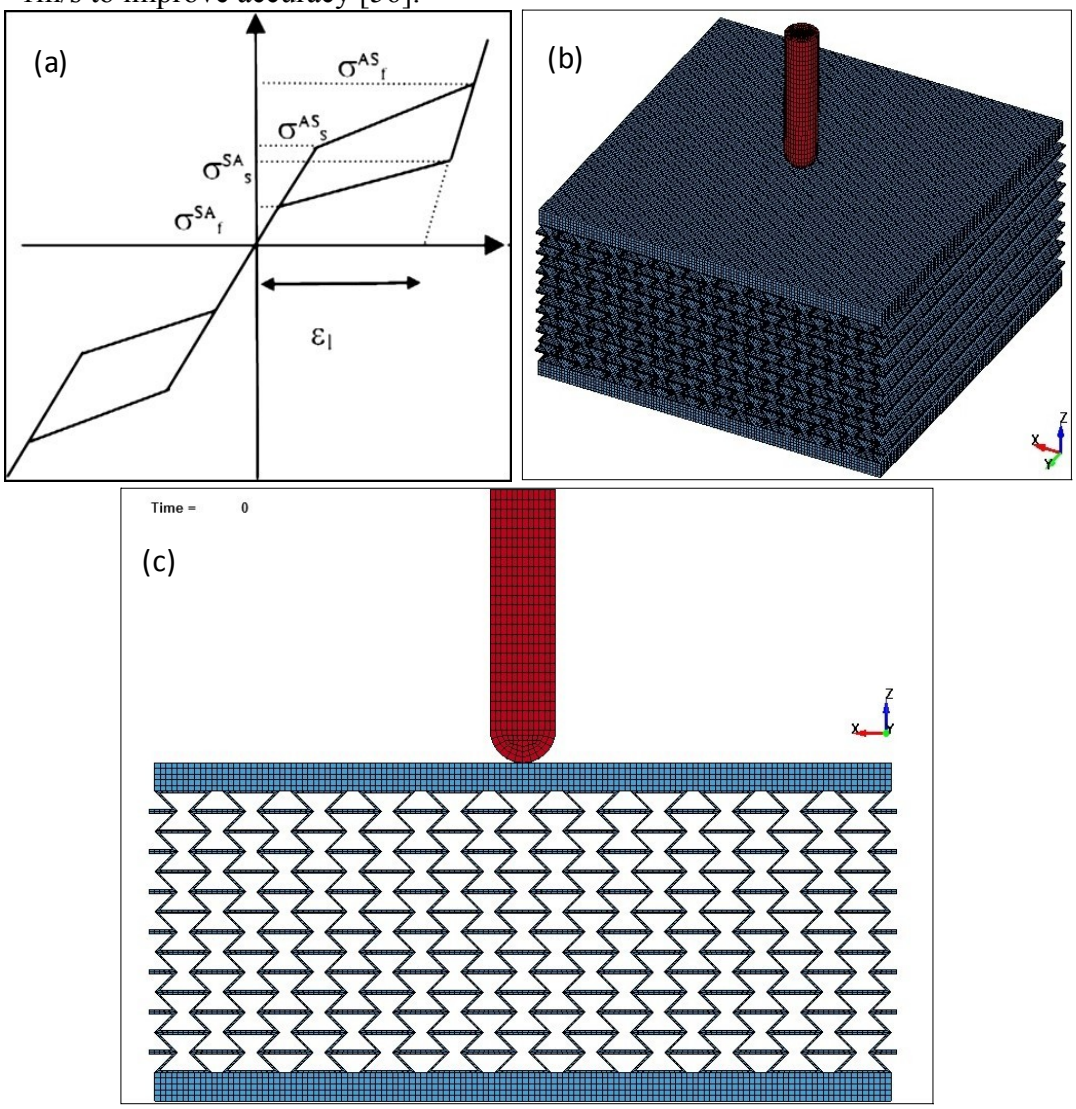

Figure 5: (a) A typical stress-strain diagram of NiTi SMA, (b) Isometric view of the meshed model, (c) front view of the meshed model

3. Results and Discussion

3.1.Impact Simulation using Solid Plates

For the mild steel solid plate, experimental data from literature was used for model validation. In Figure 6a, a comparison between internal energy and hourglass energy is reported. It can be seen that the hourglass energy was much less than internal energy peak as a result of implementing the hourglass control, which shows a reliable model. The impact velocity was 821 m/s, for which the experimental residual velocity was 758.6 m/s [50]. The numerical

residual velocity was found 789.3 m/s, which represents an error of 4.05% compared to the experimental results. The predicted results can also be compared with other numerical studies reported by Raguraman and co-authors [52] who used a rigid projectile core and shell elements for the plate. In Raguraman et al. study, the projectile completely left the plate after 39 ms. Similar results were obtained in the current study where 41 ms were needed for the projectile to completely penetrate the plate. The damage left by the projectile when impacted the model configuration as presented in [52] is shown in Figure 6b. The damage tends to have a nearcircular geometry with 6.66 mm diameter. Similar to the experimental results, the projectile was perpendicular to the plate after the impact, and the plate tended to have major damage at the rear face.

(a)

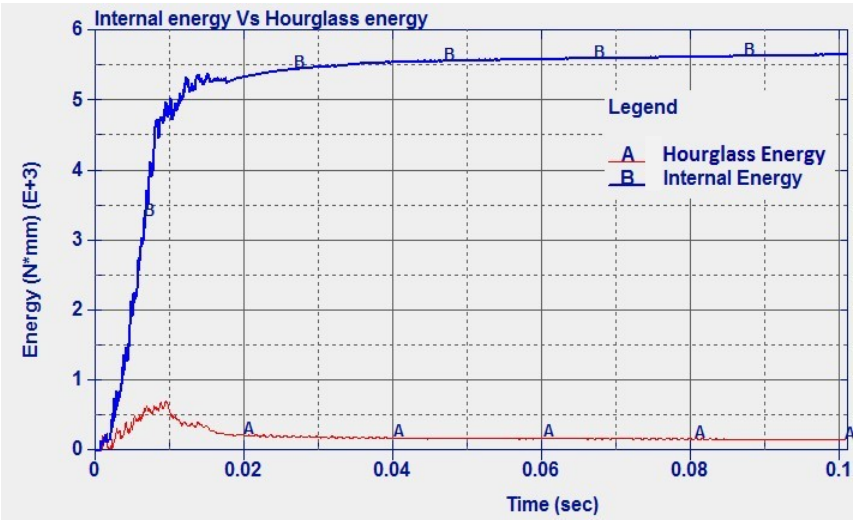

(b)

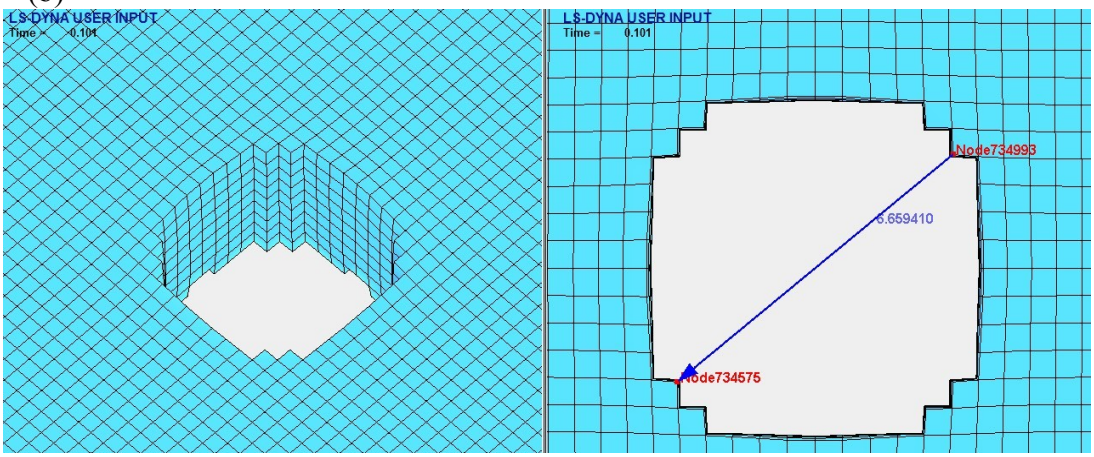

Figure 6: (a) Internal energy vs Hourglass energy, (b) the 3D and 2D damage marks of the projectile penetrating the solid steel plate.

The history of the velocity and the kinetic energy of the projectile is shown in Figure 7. From Figure 7b, it can be noted that the initial kinetic energy is 1.769 x10^6 N.mm and the numerical final kinetic energy is 1.635 x10^6 N.mm. The difference between the final and initial kinetic energies represents the numerical energy absorbed by the solid plate, and its value is 1.34 x10^5 N.mm.

(a)

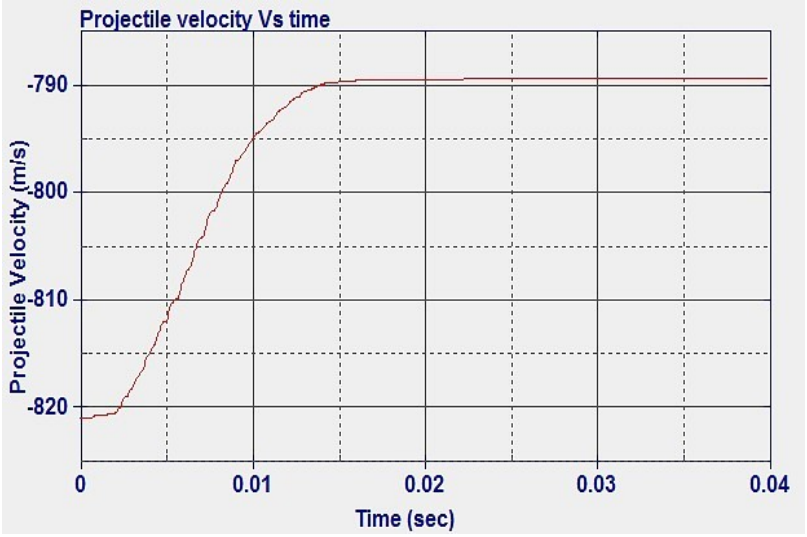

(b)

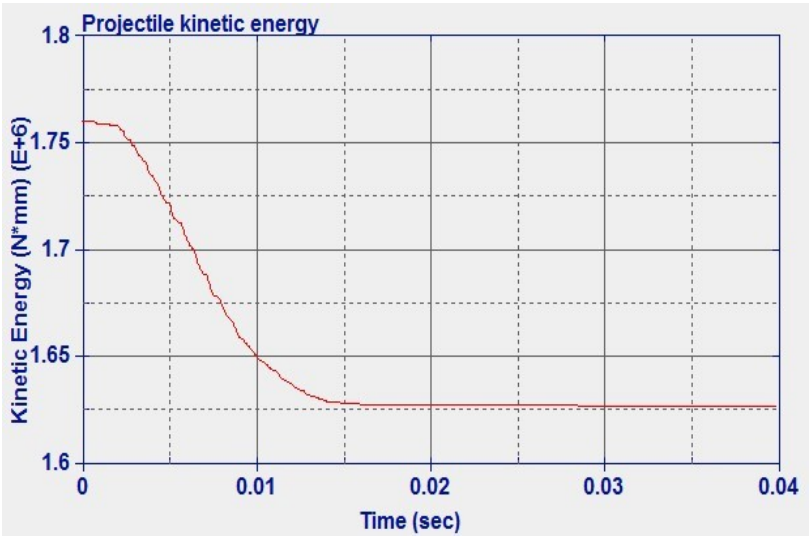

Figure 7: Steel solid plate: (a) Projectile velocity vs time, (b) Kinetic Energy vs time.

Next, the steel plate was replaced with NiTi plate to investigate the effect of using NiTi. The impact velocity was 821 m/s, for which the numerical residual velocity was 747 m/s. As shown in Figure 8, greater internal and hourglass energy were predicted compared with those in case of steel. The hourglass energy was still less than 10% of the internal energy peak owing to the implemented hourglass control, see Figure 8a. The damage left by the projectile was smaller than that in case of steel with 6.02 mm in diameter compared to 6.66 mm in diameter when the steel plate was used as shown in Figure 8b. Figure 9 presents the variation of the velocity and the kinetic energy of the projectile over time. As shown, the initial projectile kinetic energy is

1.769 x10^6 N.mm. The difference between the initial numerical kinetic energy and the final kinetic energy represents the numerical energy absorbed by the plate, which is 3.06 x10^5 N.mm.

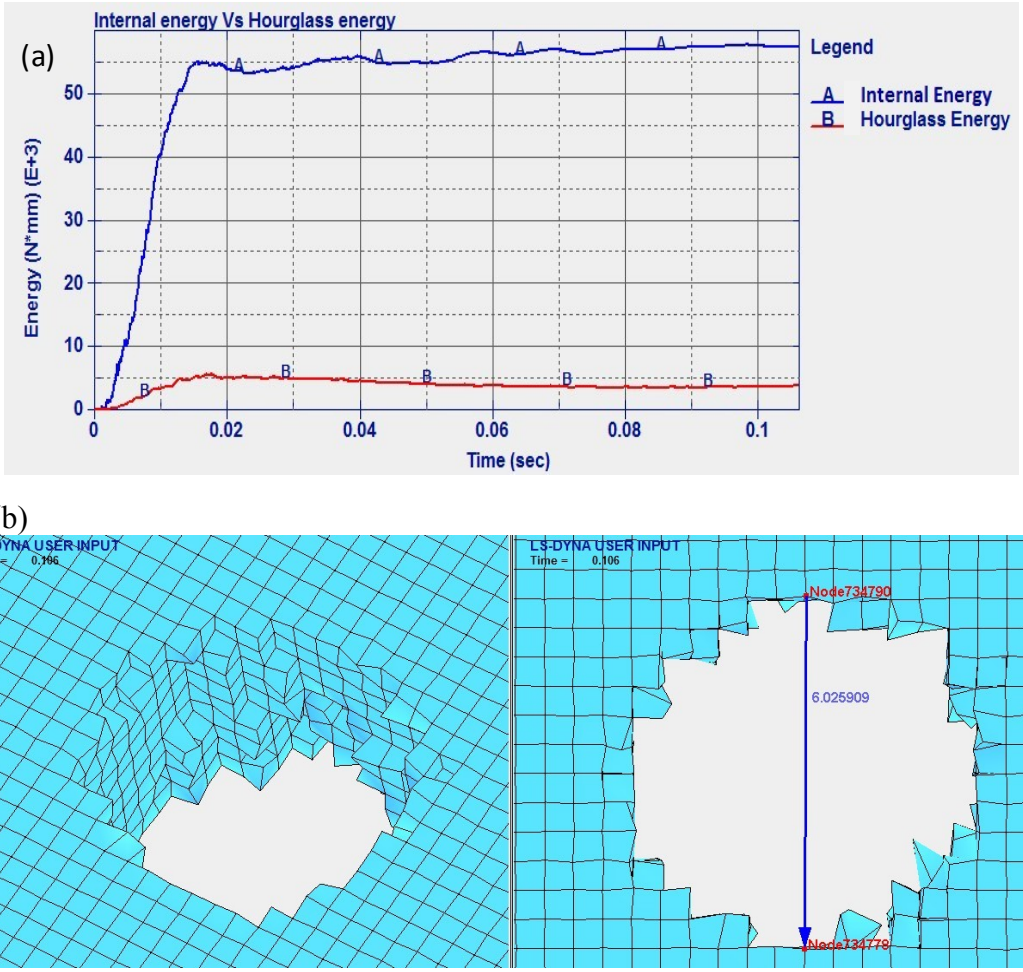

Figure 8: (a) Internal energy vs Hourglass energy, (b) the 3D and 2D damage marks of the projectile penetrating the NiTi plate.

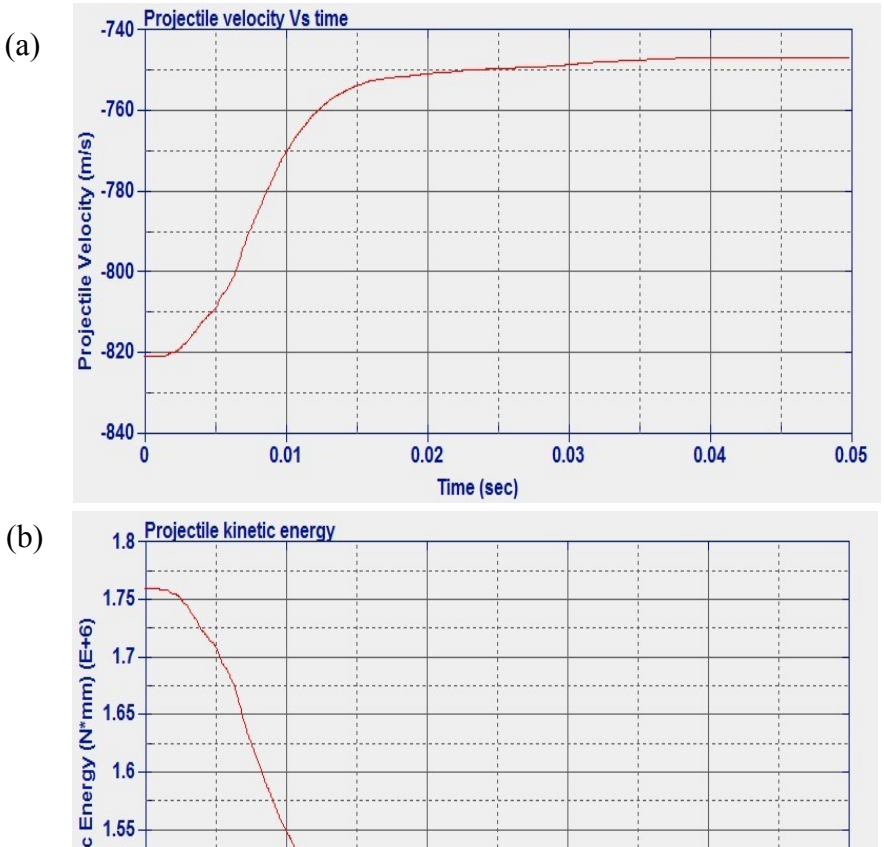

Figure 9: N gy Vs time.

Table 4 shows a comparison between the ballistic performance of both the steel and NiTi. It is clear that the NiTi plate experienced better ballistic behaviour when hit by a high-speed projectile. The residual velocity of the projectile and the damage in the target were lower than in steel plate. As a result, the absorbed energy by the plate was higher. An important conclusion is that absorbed energy by a unit mass of NiTi is about 2.7 times those in steel.

Table 4: Comparison between steel and NiTi shape memory alloy plate

	Steel	NiTi
Weight of the target (g)	1468	1212.6
Thickness (mm)	4.7	4.7
The residual velocities (mm/sec)	758	746
The energy absorbed (N.mm)	$1.34x10^5$	$3.06x10^5$
Energy absorbed by unit mass (N.mm/g)	91.28	252.35
Damage (mm)	6.66	6.02

3.2.Optimisation of Poisson's Ratio and Validation

Figure 10 shows the analytically calculated Poisson's ratio for different unit cell parameters. As shown, the values were obtained of the Poisson's ratio (from equation 1) and plotted against the cell angle for different aspect ratio α and density β. The curves were interrupted for cell angles lower than the critical angle introduced in equation 2 γ_{min}. It can be noted that the negative cell angle resulted in a negative Poisson's ratio. In addition, small and negative cell angles combined with low aspect ratio would result in increasing the negative Poisson's ratio. Furthermore, the Poisson's ratio had direct relationships with both α and β. By increasing the aspect ratio from 1.2 to 2 (at a cell angle of -30° and a relative density of 0.2) the Poisson's ratio increased from -1.84 to -0.86. On the other hand, increasing the relative density from 0.1 to 0.25 (at a cell angle of -40° and an aspect ratio of 1.5) increased the Poisson's ratio from 1.04 to -0.91. This means that not only the cell angle but also the other

geometric cell parameters can dominate the values of the re-entrant structure Poisson's ratio. Finally, it should be emphasized that as the values of the relative density in this work were relatively small

($\beta \leq 0.25$) the deflection of the walls can be neglected [46]. From the results of the analytical model, the cell parameters that yielded the minimum Poisson's ratio were found to be $\alpha=1.2$, $\beta=0.08$ and $\gamma= -30°$. The corresponding Poisson's ratio was calculated to be -2.089. These values of cell parameters were used further during the FE modelling and experimental study.

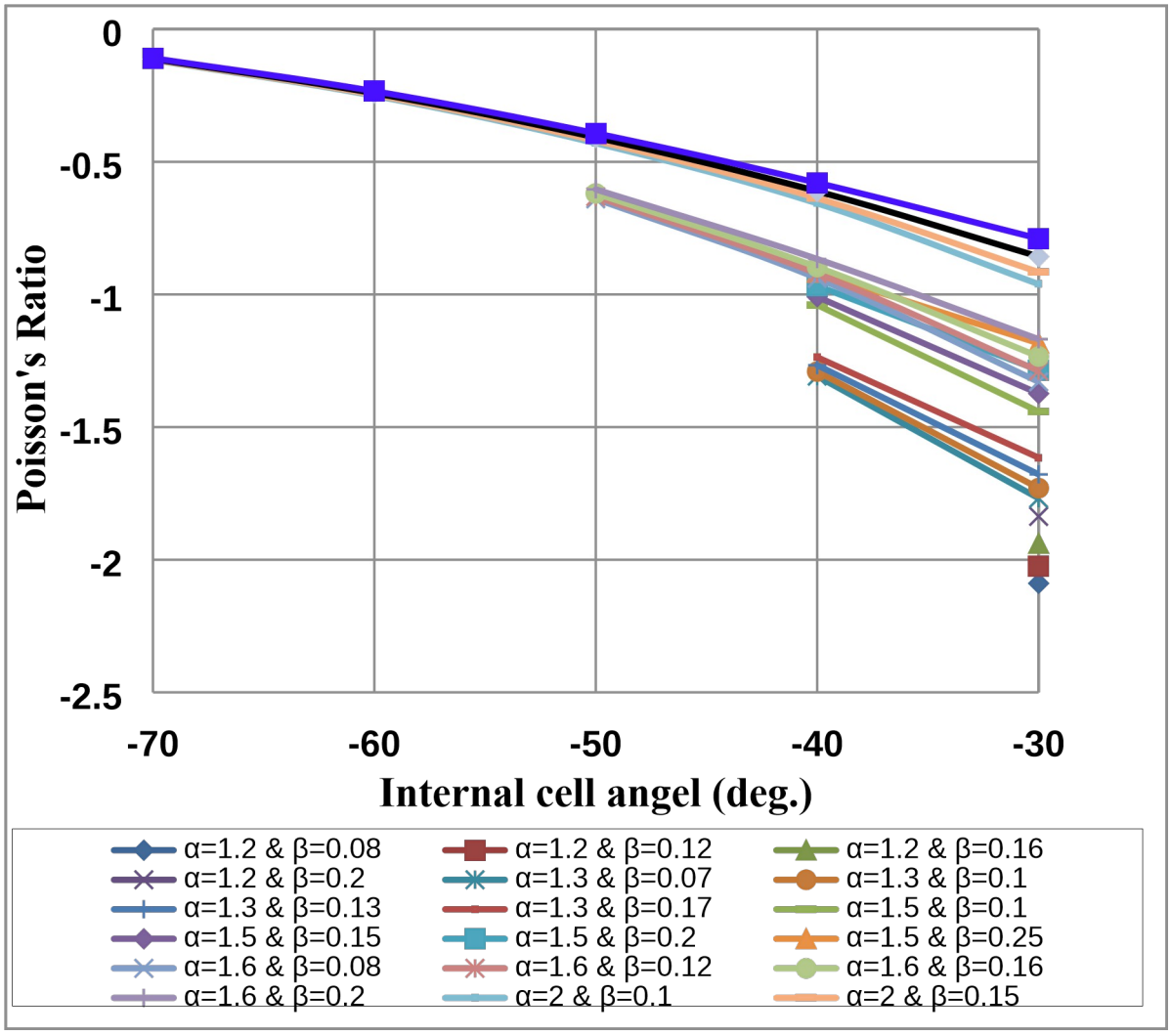

Figure 10: In-plane Poisson's ratio calculations as a function of cell dimensions

Figure 11 shows the DCS, force-displacement and the experimental and the simulated transverse strain against the axial strain for the re-entrant auxetics structure. The DSC curve of the fabricated sample demonstrates the phase transformation from austenite and martensitic during heating and cooling. Overall, the results showed that the sample preserved the shape memory characteristics of NiTi, Figure 11a. The maximum compressive force for the samples was 10 KN, Figure 11b. Following the compression, the deformed structure was heated to 100 °C, which led to the restoration of the original (undeformed) geometry. Figure 11c shows a good agreement between the experimental and simulation results. The calculated Poisson's ratio was obtained by determining the slope of the simulation and experimental lines. The

Poisson's ratio of simulation results is -2.04, whereas it is -1.98 from the experimental results. The results show an acceptable modelling error of <5% between the experimental and simulation values. In addition, the simulation and the experimentally obtained data are close to the analytically obtained in-plane Poisson's ratio of -2.089. The agreement between the analytical, simulation and the literature results enabled the progression of the ballistic modelling.

(a)

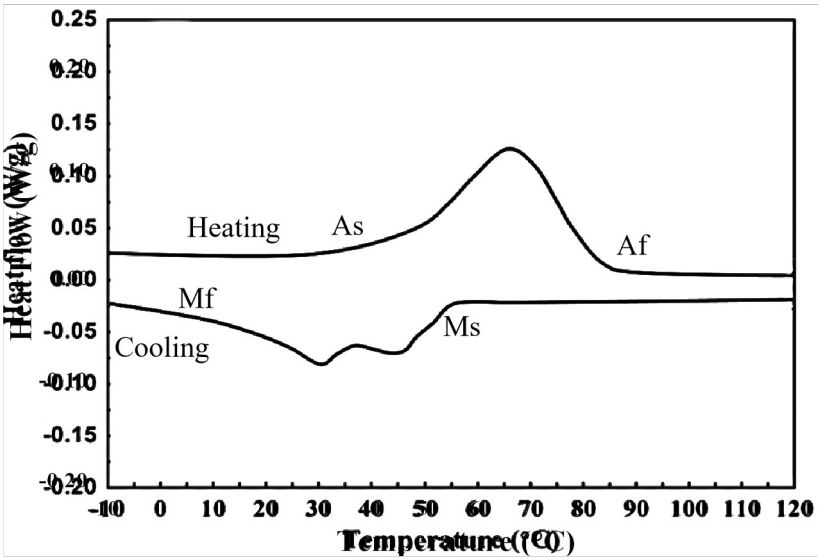
Heating
As
Af
Mf
Ms
Cooling
0.25
0.15
0.05
-0.05
-0.15
-10
0
10
20
30
40
50
60
70
80
90
100
110
120

(b)

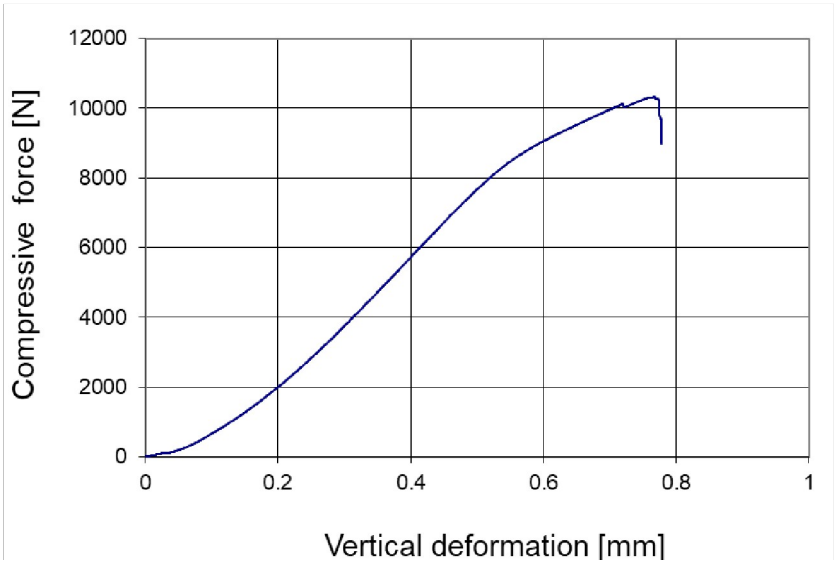
Compressive force [N]
12000
10000
8000
6000
4000
2000
0
0
0.2
0.4
0.6
0.8
1
Vertical deformation [mm]

(c)

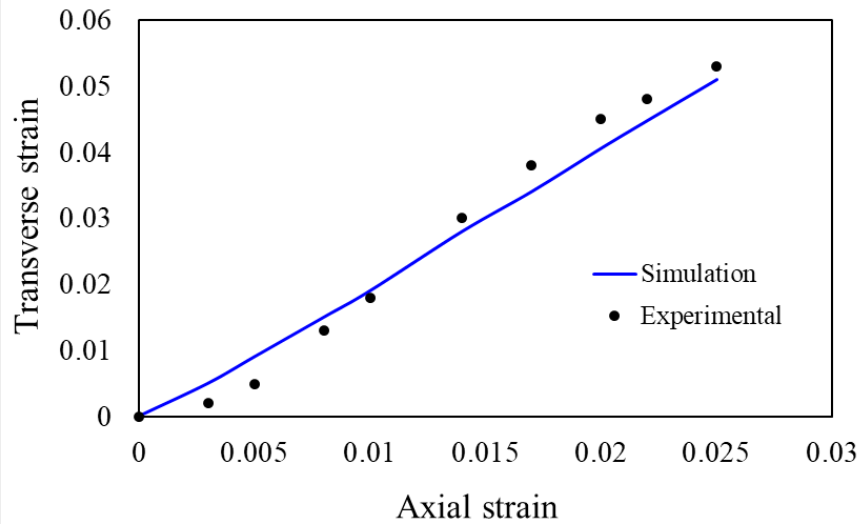

Figure 11: (a) DSC curve of the fabricated sample, (b) Force-displacement curve of one of the fabricated samples using compression testing, (c) Experimental and simulated compressive transverse strain versus compressive axial strain for the NiTi auxetic structure.

3.3.Impact Simulation using NiTi Auxetic structure

In this section, the re-entrant auxetic structure with the optimum parameters was employed with solid facets on top and bottom, as represented in Figure 5c. The auxetic structure is 20 mm height plus top and bottom plates each with 2 mm thickness. Different impact velocities (Vi), ranged from 875 to 900 m/s, were used and the energy absorption and the residual velocity during the impact were calculated. The evolution of the projectile velocity at several impact velocities was depicted as a function of time in the following set of figures. Figures of two projectile velocities of 875 to 900 m/s were presented to avoid repeatability. The total time was estimated to have a maximum of 0.16, which can be defined as the time when the projectile touches the top plate and the time at which the projectile pierces the structure.

Figure 12 presents the changes in the projectile velocity as the time of the impact increases. The energy absorbed per unit mass was determined to be 495 N.mm/g. On the other hand, Figure 13 shows the deformation of the SMA plate during the impact at different time steps from 0.002 to 0.078 ms. The simulation was repeated at a projectile speed of 900 m/s. The projectile velocity and the energy values in the plate during the impact are given in Figure 14. In this case, the energy absorbed per unit mass was 521 N.mm/g. Furthermore, the

deformation of the SMA auxetic structure during the impact at different time steps from 0.002 to 0.111ms is shown in Figure 15.

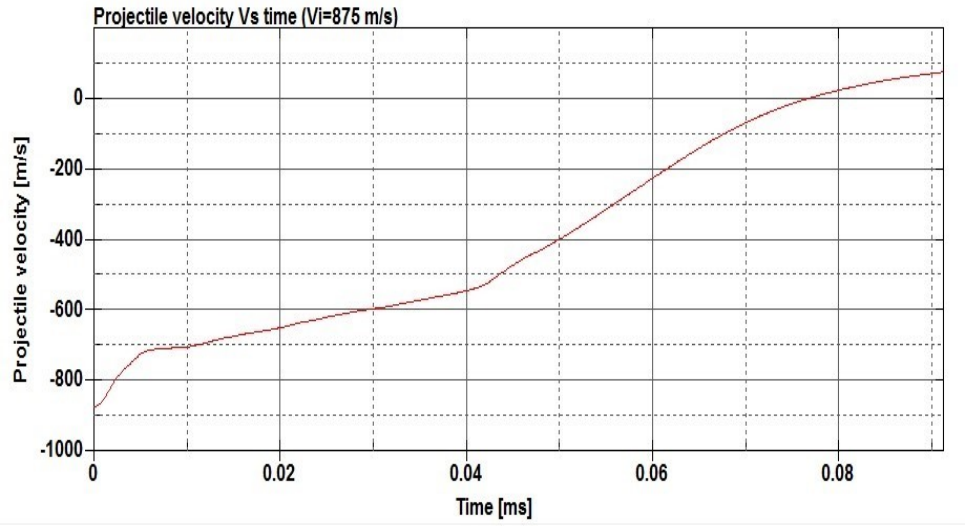

Figure 12: Projectile velocity Vs time for the NiTi auxetic structure at a projectile speed of 875 mm/s

.

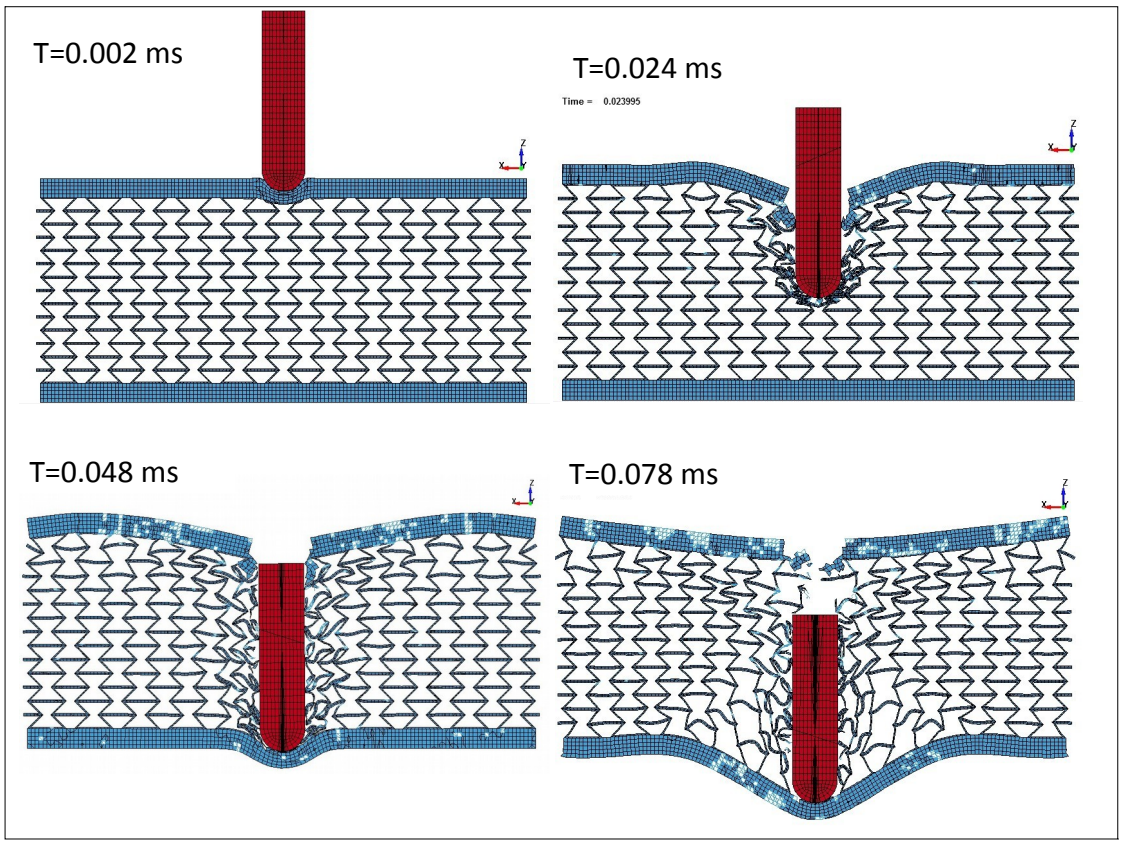

Figure 13: Structure deformation at different timing, Vi= 875 m/s

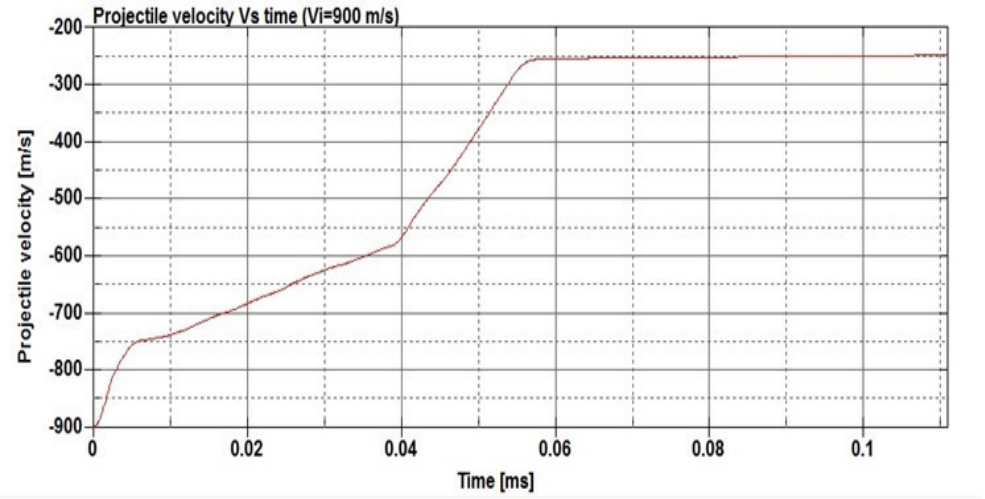

Figure 14: Projectile velocity Vs time for the NiTi auxetic structure at a projectile speed of 900 mm/s

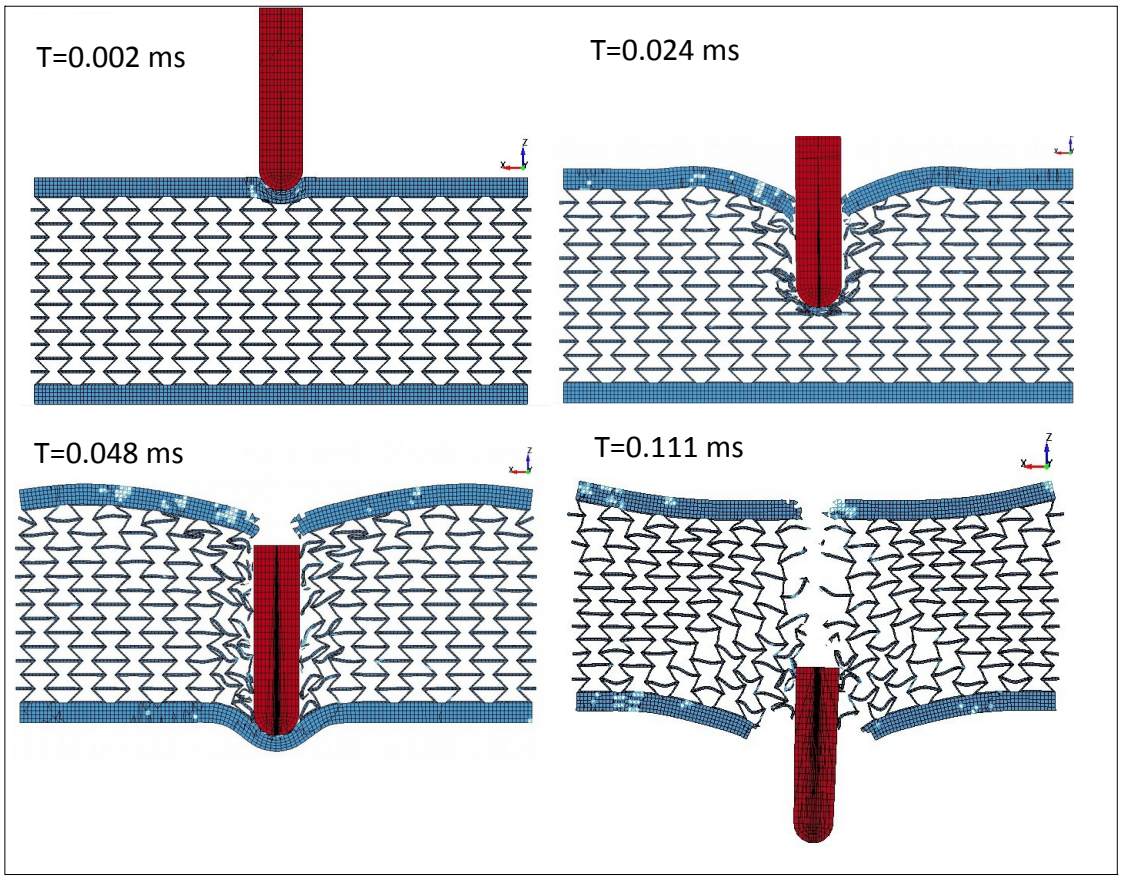

Figure 15: Structure deformation at different timing, Vi= 900 m/s

Figure 12 to Figure 15 show that there are three different stages can be identified during the penetration process of the projectile into the auxetic structure and they are; The top plate, auxetic structure, and bottom plate. In stage 1, at the beginning of the impact event, the top plate caused a sudden drop in the projectile velocity, so that the projectile approached the

auxetic structure at a velocity of about 420 m/s. In stage 2, auxetic structure became denser in the region around the projectile and hence the projectile velocity decreased as the projectile penetrated through the auxetic structure. It can be concluded that the auxetic structure tends to get closer and denser trying to resist the penetration of the projectile, which is very important to absorb more energy from the projectile impact. In stage 3, an additional drop in the projectile velocity was caused by the bottom plate. It can be noted that, the developed internal energy in the structure increases when the projectile impact speed increases. The ballistic limit of the structure, which is the velocity at which the projectile cannot penetrate, through the whole armour layer, can be calculated. In other words, the residual velocity of projectile becomes zero when the impact velocity of the projectile is lower than the ballistic limit. In this case, at a projectile impact speed 875 m/s, the projectile velocity reached zero m/s at the time of 0.078 ms and the projectile could not pierce into the armour structure. The calculated energy absorbed by unit mass, in this case, is 495 N.mm/g compared to 91.28 N.mm/g and 252.35 N.mm/g for steel and NiTi solid plates, respectively. Finally, at higher speeds, the projectile could pierce the structure and leave with a residual velocity.

4. Conclusion

This paper introduced a metamaterial, which combines the shape memory/superelasticity and the negative Poisson's ratio properties and proved to have higher ballistic performance when compared to conventional steel armours. An analytical model was firstly used to optimise the geometrical parameters of the re-entrant auxetic structure. It was found that re-entrant auxetic structure with a cell angle of -30° produced the highest Poisson's of -2.089. 4D printing process using PBF was used to fabricate the optimised auxetic structure using gas atomised NiTi powder. The obtained Poisson's ratio of the fabricated auxetic structure was found in agreement with both the analytical model and the finite element simulation. A finite element model was developed of a hard steel core projectile and both NiTi and steel solid plates to understand the effect of using NiTi when compared to the conventional steel material. The

results show that NiTi proved to have a better performance than steel. The impact processes were also simulated to the optimised auxetic NiTi structure at different projectile speeds using a nonlinear FE code. Three stages of the impact process describing the penetration of the top plate, auxetic structure, and bottom plate were clearly identified. The results also show that the optimised auxetic structures affect the dynamic response of the projectile by getting denser towards the impact location. This helped to improve the energy absorbed by unit mass from 91.28 N.mm/g and 252.35 N.mm/g in case of solid steel and solid NiTi, respectively, to 495 N.mm/g for the optimised NiTi auxetic structure. Future studies will include the implementation of the developed Auxetic structure into existing armours designs. The ballistic performance will be experimentally investigated with projectiles at different speeds, and the compression characterisation will be studied at different strain rates to capture the implications and limitations of the developed metamaterial.

References

[1] J.L. Williams, J.L. Lewis, (1982) Properties and an anisotropic model of cancellous bone from the proximal tibial epiphysis, J Biomech Eng, 104 50-56.

[2] R. Gatt, M. Vella Wood, A. Gatt, F. Zarb, C. Formosa, K.M. Azzopardi, A. Casha, T.P. Agius, P. Schembri-Wismayer, L. Attard, N. Chockalingam, J.N. Grima, (2015) Negative Poisson's ratios in tendons: An unexpected mechanical response, Acta Biomater, 24 201-208.

[3] H. Kimizuka, H. Kaburaki, Y. Kogure, (2000) Mechanism for negative poisson ratios over the alpha- beta transition of cristobalite, SiO2: A molecular-dynamics study, Phys Rev Lett, 84 5548-5551.

[4] M. Sanami, N. Ravirala, K. Alderson, A. Alderson, (2014) Auxetic materials for sports applications, Procedia Engineering, 72 453-458.

[5] L. Santo, (2016) Shape memory polymer foams, Progress in Aerospace Sciences, 81 6065.

[6] F. Scarpa, (2008) Auxetic materials for bioprostheses [In the Spotlight], Signal Processing Magazine, IEEE, 25 128-126.

[7] L. Boldrin, S. Hummel, F. Scarpa, D. Di Maio, C. Lira, M. Ruzzene, C.D.L. Remillat, T.C. Lim, R. Rajasekaran, S. Patsias, (2016) Dynamic behaviour of auxetic gradient composite hexagonal honeycombs, Composite Structures, 149 114-124.

[8] M.H. Hajmohammad, A.H. Nouri, M.S. Zarei, R. Kolahchi, (2019) A new numerical approach and visco-refined zigzag theory for blast analysis of auxetic honeycomb plates integrated by multiphase nanocomposite facesheets in hygrothermal environment, Engineering with Computers, 35 1141-1157.

[9] G. Imbalzano, P. Tran, T.D. Ngo, P.V.S. Lee, (2016) A numerical study of auxetic composite panels under blast loadings, Composite Structures, 135 339-352.

[10] J. Schultz, (2011) Modeling and finite element analysis methods for the dynamic crushing of honeycomb cellular meso-structures.

[11] C. Qi, S. Yang, D. Wang, L.-J. Yang, (2013) Ballistic resistance of honeycomb sandwich panels under in-plane high-velocity impact, The Scientific World Journal, 2013.
[12] G. Imbalzano, P. Tran, T.D. Ngo, P.V.S. Lee, (2017) Three-dimensional modelling of auxetic sandwich panels for localised impact resistance, Journal of Sandwich Structures and Materials, 19 291-316.
[13] W.A. Gooch Jr, (2011) Potential applications of titanium alloys in armor aystems, in: Titanium 2011 International Titanium Association, San Diego, California.
[14] N. Chan, K.E. Evans, (1997) Fabrication methods for auxetic foams, Journal of Materials Science, 32 5945-5953.
[15] R.S. Webber, K.L. Alderson, K.E. Evans, (2008) A novel fabrication route for auxetic polyethylene, part 2: Mechanical properties, Polymer Engineering and Science, 48 13511358.
[16] Y. Yao, Y. Luo, Y. Xu, B. Wang, J. Li, H. Deng, H. Lu, (2018) Fabrication and characterization of auxetic shape memory composite foams, Composites Part B: Engineering, 152 1-7.
[17] A.D. Lantada, A. de Blas Romero, M. Schwentenwein, C. Jellinek, J. Homa, (2016) Lithography-based ceramic manufacture (LCM) of auxetic structures: present capabilities and challenges, Smart Materials and Structures, 25 054015.
[18] B. Xu, F. Arias, S.T. Brittain, X.-M. Zhao, B. Grzybowski, S. Torquato, G.M. Whitesides, (1999) Making negative Poisson's ratio microstructures by soft lithography, Advanced Materials, 11 1186-1189.
[19] H. Hassanin, K. Jiang, (2009) Alumina composite suspension preparation for softlithography microfabrication, Microelectronic Engineering, 86 929-932.
[20] H. Hassanin, K. Jiang, (2013) Fabrication and characterization of stabilised zirconia micro parts via slip casting and soft moulding, Scripta Materialia, 69 433-436.
[21] H. Hassanin, K. Jiang, (2009) Fabrication of Al2O3/SiC Composite Microcomponents using Nonaqueous Suspension, Advanced Engineering Materials, 11 101-105.
[22] H. Hassanin, K. Jiang, (2011) Multiple replication of thick PDMS micropatterns using surfactants as release agents, Microelectronic Engineering, 88 3275-3277.
[23] H. Hassanin, K. Jiang, (2013) Net shape manufacturing of ceramic micro parts with tailored graded layers, Journal of Micromechanics and Microengineering, 24 015018.
[24] Z. Zhu, H. Hassanin, K. Jiang, (2010) A soft moulding process for manufacture of netshape ceramic microcomponents, The International Journal of Advanced Manufacturing Technology, 47 147-152.
[25] M.A. El-Sayed, H. Hassanin, K. Essa, (2016) Bifilm defects and porosity in Al cast alloys, The International Journal of Advanced Manufacturing Technology, 86 1173-1179.
[26] H. Hassanin, K. Jiang, (2010) Functionally graded microceramic components, Microelectronic Engineering, 87 1610-1613.
[27] K. Essa, F. Modica, M. Imbaby, M.A. El-Sayed, A. ElShaer, K. Jiang, H. Hassanin, (2017) Manufacturing of metallic micro-components using hybrid soft lithography and micro-electrical discharge machining, The International Journal of Advanced Manufacturing Technology, 91 445-452.
[28] H. Hassanin, K. Jiang, (2010) Optimized process for the fabrication of zirconia micro parts, Microelectronic Engineering, 87 1617-1619.
[29] M.A. El-Sayed, H. Hassanin, K. Essa, (2016) Effect of casting practice on the reliability of Al cast alloys, International Journal of Cast Metals Research, 29 350-354.
[30] C. Qiu, N.J.E. Adkins, H. Hassanin, M.M. Attallah, K. Essa, (2015) In-situ shelling via selective laser melting: Modelling and microstructural characterisation, Materials & Design, 87 845-853.
[31] H. Hassanin, Y. Alkendi, M. Elsayed, K. Essa, Y. Zweiri, (2020) Controlling the properties of additively manufactured cellular structures using machine learning approaches, Advanced Engineering Materials, 22 1901338.

[32] H. Hassanin, K. Essa, C. Qiu, M. Abdelhafeez Ali, J.E. Adkins Nicholas, M. Attallah Moataz, (2017) Net-shape manufacturing using hybrid selective laser melting/hot isostatic pressing, Rapid Prototyping Journal, 23 720-726.
[33] K. Essa, R. Khan, H. Hassanin, M.M. Attallah, R. Reed, (2016) An iterative approach of hot isostatic pressing tooling design for net-shape IN718 superalloy parts, The International Journal of Advanced Manufacturing Technology, 83 1835-1845.
[34] K. Essa, H. Hassanin, M.M. Attallah, N.J. Adkins, A.J. Musker, G.T. Roberts, N. Tenev, M. Smith, (2017) Development and testing of an additively manufactured monolithic catalyst bed for HTP thruster applications, Applied Catalysis A: General, 542 125-135.
[35] H. Klippstein, H. Hassanin, A. Diaz De Cerio Sanchez, Y. Zweiri, L. Seneviratne, (2018) Additive manufacturing of porous structures for unmanned aerial vehicles applications, Advanced Engineering Materials, 20 1800290.
[36] Y. Li, Z. Feng, L. Huang, K. Essa, E. Bilotti, H. Zhang, T. Peijs, L. Hao, (2019) Additive manufacturing high performance graphene-based composites: A review, Composites Part A: Applied Science and Manufacturing, 124 105483.
[37] H. Hassanin, L. Finet, S.C. Cox, P. Jamshidi, L.M. Grover, D.E.T. Shepherd, O. Addison, M.M. Attallah, (2018) Tailoring selective laser melting process for titanium drugdelivering implants with releasing micro-channels, Additive Manufacturing, 20 144-155. [38] H. Klippstein, A. Diaz De Cerio Sanchez, H. Hassanin, Y. Zweiri, L. Seneviratne, (2018) Fused deposition modeling for unmanned aerial vehicles (uavs): A review, Advanced Engineering Materials, 20 1700552.
[39] A. Galatas, H. Hassanin, Y. Zweiri, L. Seneviratne, (2018) Additive manufactured sandwich composite/ABS parts for unmanned aerial vehicle applications, Polymers, 10 1262.
[40] A. Sabouri, A.K. Yetisen, R. Sadigzade, H. Hassanin, K. Essa, H. Butt, (2017) ThreeDimensional Microstructured Lattices for Oil Sensing, Energy & Fuels, 31 2524-2529.
[41] Y.Y.C. Choong, S. Maleksaeedi, H. Eng, S. Yu, J. Wei, P.-C. Su, (2020) High speed 4D printing of shape memory polymers with nanosilica, Applied Materials Today, 18 100515.
[42] Y.Y.C. Choong, S. Maleksaeedi, H. Eng, J. Wei, P.-C. Su, (2017) 4D printing of high performance shape memory polymer using stereolithography, Materials & Design, 126 219225.
[43] S. Li, H. Hassanin, M.M. Attallah, N.J.E. Adkins, K. Essa, (2016) The development of TiNi-based negative Poisson's ratio structure using selective laser melting, Acta Materialia, 105 75-83.
[44] C. Tan, S. Li, K. Essa, P. Jamshidi, K. Zhou, W. Ma, M.M. Attallah, (2019) Laser powder bed fusion of Ti-rich TiNi lattice structures: process optimisation, geometrical integrity, and phase transformations, International Journal of Machine Tools and Manufacture, 141 19-29.
[45] S. Li, H. Hassanin, M.M. Attallah, N.J. Adkins, K. Essa, (2016) The development of TiNi-based negative Poisson's ratio structure using selective laser melting, Acta Materialia, 105 75-83.
[46] F. Scarpa, P. Panayiotou, G. Tomlinson, (2000) Numerical and experimental uniaxial loading on in-plane auxetic honeycombs, The Journal of Strain Analysis for Engineering Design, 35 383-388.
[47] L.J. Gibson, M.F. Ashby, (1982) The mechanics of three-dimensional cellular materials, in: Proceedings of the Royal Society of London A: Mathematical, Physical and Engineering Sciences, The Royal Society, pp. 43-59.
[48] N. RG, C. Venkatesha, R. Jain, (2012) Numerical simulation of soft-body impact on Shape Memory Alloys (SMA), International Journal of Scientific & Engineering Research, 3. [49] J.O. Hallquist, L.-D.T. Manual, (2007) Livermore Software Technology Corporation, Livermore, Ca.
[50] N. Kılıç, B. Ekici, (2013) Ballistic resistance of high hardness armor steels against 7.62 mm armor piercing ammunition, Materials & Design, 44 35-48.

[51] N. Gupta, V. Madhu, (1997) An experimental study of normal and oblique impact of hard-core projectile on single and layered plates, International journal of impact engineering, 19 395-414.
[52] M. Raguraman, A. Deb, N. Gupta, (2007) A numerical study of projectile impact on mild steel armour plates, Current Science, 93 498-506.
[53] M. Raguraman, A. Deb, (2006) Accurate prediction of projectile residual velocity for impact on single and multi-layered steel and aluminum plates, in: 9th International LSDYNA Users Conference, Hyatt Regency Dearborn Dearborn, Michigan USA.
[54] S. Bala, J. Day, (2012) General guidelines for crash analysis in LS-DYNA, Livermore Software Technology Corporation.
[55] M. Meo, F. Marulo, M. Guida, S. Russo, (2013) Shape memory alloy hybrid composites for improved impact properties for aeronautical applications, Composite Structures, 95 756766.
[56] A. Serjouei, R. Chi, Z. Zhang, I. Sridhar, (2015) Experimental validation of BLV model on bi-layer ceramic-metal armor, International Journal of Impact Engineering, 77 30-41.